The Astrophysical Journal Supplement Series, 257:7 (14pp), 2021 November https://doi.org/10.3847/1538-4365/ac1435
© 2021. The American Astronomical Society. All rights reserved.

Molecules with ALMA at Planet-forming Scales (MAPS). VII. Substellar O/H and C/H and Superstellar C/O in Planet-feeding Gas

Arthur D. Bosman[1], Felipe Alarcón[1], Edwin A. Bergin[1], Ke Zhang[1,2,22], Merel L. R. van't Hoff[1], Karin I. Öberg[3], Viviana V. Guzmán[4], Catherine Walsh[5], Yuri Aikawa[6], Sean M. Andrews[3], Jennifer B. Bergner[7,23], Alice S. Booth[5,8], Gianni Cataldi[6,9], L. Ilsedore Cleeves[10], Ian Czekala[11,12,13,14,15,23], Kenji Furuya[9], Jane Huang[1,3,23], John D. Ilee[5], Charles J. Law[3], Romane Le Gal[3,16,17,18], Yao Liu[19], Feng Long[3], Ryan A. Loomis[20], François Ménard[16], Hideko Nomura[9], Chunhua Qi[3], Kamber R. Schwarz[21,23], Richard Teague[3], Takashi Tsukagoshi[9], Yoshihide Yamato[6], and David J. Wilner[3]

[1] Department of Astronomy, University of Michigan, 323 West Hall, 1085 S. University Ave., Ann Arbor, MI 48109, USA; arbos@umich.edu
[2] Department of Astronomy, University of Wisconsin–Madison, 475 N. Charter St., Madison, WI 53706, USA
[3] Center for Astrophysics | Harvard & Smithsonian, 60 Garden St., Cambridge, MA 02138, USA
[4] Instituto de Astrofísica, Pontificia Universidad Católica de Chile, Av. Vicuña Mackenna 4860, 7820436 Macul, Santiago, Chile
[5] School of Physics and Astronomy, University of Leeds, Leeds LS2 9JT, UK
[6] Department of Astronomy, Graduate School of Science, The University of Tokyo, Tokyo 113-0033, Japan
[7] University of Chicago Department of the Geophysical Sciences, Chicago, IL 60637, USA
[8] Leiden Observatory, Leiden University, 2300 RA Leiden, The Netherlands
[9] National Astronomical Observatory of Japan, 2-21-1 Osawa, Mitaka, Tokyo 181-8588, Japan
[10] University of Virginia, 530 McCormick Rd., Charlottesville, VA 22904, USA
[11] Department of Astronomy and Astrophysics, 525 Davey Laboratory, The Pennsylvania State University, University Park, PA 16802, USA
[12] Center for Exoplanets and Habitable Worlds, 525 Davey Laboratory, The Pennsylvania State University, University Park, PA 16802, USA
[13] Center for Astrostatistics, 525 Davey Laboratory, The Pennsylvania State University, University Park, PA 16802, USA
[14] Institute for Computational & Data Sciences, The Pennsylvania State University, University Park, PA 16802, USA
[15] Department of Astronomy, 501 Campbell Hall, University of California, Berkeley, CA 94720-3411, USA
[16] Univ. Grenoble Alpes, CNRS, IPAG, F-38000 Grenoble, France
[17] IRAP, Université de Toulouse, CNRS, CNES, UT3, 31400 Toulouse, France
[18] IRAM, 300 rue de la piscine, F-38406 Saint-Martin d'Hères, France
[19] Purple Mountain Observatory & Key Laboratory for Radio Astronomy, Chinese Academy of Sciences, Nanjing 210023, People's Republic of China
[20] National Radio Astronomy Observatory, Charlottesville, VA 22903, USA
[21] Lunar and Planetary Laboratory, University of Arizona, 1629 E. University Blvd., Tucson, AZ 85721, USA
Received 2021 February 15; revised 2021 June 10; accepted 2021 June 14; published 2021 November 3

Abstract

The elemental composition of the gas and dust in a protoplanetary disk influences the compositions of the planets that form in it. We use the Molecules with ALMA at Planet-forming Scales (MAPS) data to constrain the elemental composition of the gas at the locations of potentially forming planets. The elemental abundances are inferred by comparing source-specific gas-grain thermochemical models with variable C/O ratios and small-grain abundances from the DALI code with CO and C_2H column densities derived from the high-resolution observations of the disks of AS 209, HD 163296, and MWC 480. Elevated C/O ratios (∼2.0), even within the CO ice line, are necessary to match the inferred C_2H column densities over most of the pebble disk. Combined with constraints on the CO abundances in these systems, this implies that both the O/H and C/H ratios in the gas are substellar by a factor of 4–10, with the O/H depleted by a factor of 20–50, resulting in the high C/O ratios. This necessitates that even within the CO ice line, most of the volatile carbon and oxygen is still trapped on grains in the midplane. Planets accreting gas in the gaps of the AS 209, HD 163296, and MWC 480 disks will thus acquire very little carbon and oxygen after reaching the pebble isolation mass. In the absence of atmosphere-enriching events, these planets would thus have a strongly substellar O/H and C/H and superstellar C/O atmospheric composition. This paper is part of the MAPS special issue of the Astrophysical Journal Supplement.

Unified Astronomy Thesaurus concepts: Abundance ratios (11); Astrochemistry (75); Protoplanetary disks (1300)

1. Introduction

More than 10% of stars are thought to host a Jupiter-sized planet (Johnson et al. 2010; Winn & Fabrycky 2015). Current observational campaigns are probing the atmospheric composition of these gas giants, with future instruments promising better characterization of more gas giants (e.g., Madhusudhan et al. 2014; Greene et al. 2016; Sing et al. 2016). These composition measurements place constraints on the process of planet formation and evolution by comparison of the composition of protoplanetary disks and the planets that formed within them (e.g., Madhusudhan et al. 2017). Achieving that goal will require measurements of the elemental composition of disks, particularly around substructures (e.g., gaps) in the millimeter disk, that are likely opened by young planets (e.g., Paardekooper & Mellema 2006; Rosotti et al. 2016; Zhang et al. 2018).

The composition of a planet is predicted to depend on the location of formation (e.g., Öberg et al. 2011; Cridland et al. 2017; Öberg & Bergin 2021), particularly relative to the ice/gas transitions (ice lines) of major volatile carriers such as CO, CO_2, H_2O, N_2, and NH_3. Further studies have shown that the transport of ices via sedimentation and inward drift of pebbles

[22] NASA Hubble Fellow.
[23] NASA Hubble Fellowship Program Sagan Fellow.

also has a significant impact on the composition of the gas and ice that can be accreted by planets (Ciesla & Cuzzi 2006; Piso et al. 2015; Booth et al. 2017; Booth & Ilee 2019; Krijt et al. 2020). All of these studies assume that the disk material has a volatile interstellar medium (ISM) elemental composition with various additional assumptions regarding chemistry and disk dynamics. The model-to-model variations create significant uncertainties for predicting planetary composition (e.g., Eistrup et al. 2016; Booth et al. 2017).

A more direct link between the composition and formation location of a giant planet could be made by comparing the elemental composition of the material at the specific radial locations or sites of planet formation with present-day gas giant exoplanet atmospheric composition. On top of this, a measurement of the elemental composition of the disk during planet formation can act as an intermediary calibration point to improve the accuracy of population synthesis models (e.g., Mordasini et al. 2009).

Accurately measuring the elemental composition of the disk requires an observational data set that covers many different molecular species, as well as a physical understanding of the regions being probed by the observations (e.g., Bergin et al. 2016; Trapman et al. 2017; Cleeves et al. 2018; Bosman et al. 2019). This limits the derivation of elemental composition to disks with a broad range of observations and a good physical model available. With the Molecules with ALMA at Planet-forming Scales (MAPS) data and ancillary modeling efforts (Öberg et al. 2021; Zhang et al. 2021)[24], the disks in the MAPS sample are perfect objects for an elemental composition study, especially as the high resolution of the data allows for a radially resolved measurement of the elemental composition.

In this paper, we will focus on the carbon and oxygen abundances, which are derived by comparison of models directly to the high-resolution MAPS data that resolve putative sites of incipient giant planet formation. The carbon and oxygen abundances in the disk will be derived using constraints on the CO column from Zhang et al. (2021) and the C_2H column from Guzmán et al. (2021). The CO is used to constrain the available total C or O column (e.g., C/H and O/H), and we use the known dependency of C_2H on the carbon-to-oxygen (C/O) ratio to determine the C/O ratio in the disk gas (e.g., Bergin et al. 2016; Miotello et al. 2019; Bosman et al. 2021). A focus on the C/O ratio in the disk gas is well matched to the available volatile abundance measurements of exoplanetary atmospheres (Madhusudhan et al. 2014; Greene et al. 2016; Madhusudhan 2019).[25]

2. Methods

2.1. Source Selection

We will focus on three of the five disks targeted by MAPS: the disks around AS 209, HD 163296, and MWC 480. All three of these disks have deep gaps in the millimeter emission indicative of ongoing planet formation (see Figure 1; Andrews et al. 2018; Guzmán et al. 2018; Huang et al. 2018; Long et al. 2018; Zhang et al. 2018; Liu et al. 2019), as well as gas velocity structures thought to be perturbations induced by unseen planets in these gaps (Pinte et al. 2018; Teague et al. 2018, 2019; Teague et al. 2021). We leave out the disks around IM Lup and GM Aur. The composition of the IM Lup disk has already been discussed in detail in Cleeves et al. (2018). The GM Aur disk is accreting new material, influencing the chemical composition of the disk (Huang et al. 2021; Schwarz et al. 2021), complicating modeling of the disk.

Furthermore, in these disks, we will focus on the gas on the scale of the millimeter disk, that is, the size of the disk in the millimeter continuum, using these large grains as a signpost of active planet formation. Figure 1 shows millimeter continuum radial profiles, rich in structure, for the three disks that are studied together with the planet masses that are inferred to cause these structures (Zhang et al. 2018; Liu et al. 2019; Sierra et al. 2021).[26] All three disks show potentially planet-induced dust structure that is clearly seen at the resolution of the MAPS continuum data ($\sim 0\farcs1 \times 0\farcs1$; Sierra et al. 2021). The MAPS data are thus able to distinguish the gap region from the surrounding disk material.

Our focus is on understanding the chemical composition of localized regions associated with incipient planet formation. In the AS 209 disk, the structures of interest are the gaps at 61 and 105 au, straddling a bright ring at 74 au (Guzmán et al. 2018). These are all well outside of the CO ice line, which is located around 15 au (Alarcón et al. 2021; Zhang et al. 2021). In the HD 163296 disk, we will focus on the dust gaps at 48 and 86 au, with one gap inside and one gap outside the ice line at 70 au (Isella et al. 2018; Zhang et al. 2020a; Calahan et al. 2021; Zhang et al. 2021). Finally, for the MWC 480 disk, we focus on the 74 au gap, which is inside the CO ice line at 100 au (Liu et al. 2019; Zhang et al. 2021). We disregard the inner ~10 au, as an accurate CO column density has not been derived for this region (Zhang et al. 2021).

To constrain the oxygen and carbon elemental abundances in the three selected disks, we base ourselves on results and models developed within the MAPS ALMA large program (Öberg et al. 2021). For C_2H, the column density derived in Guzmán et al. (2021) is used. These column densities are derived from the image cube by fitting the different C_2H hyperfine components. The C_2H column density derived from the images is uncertain within 30 au. As such, we derive a separate constraint on the C_2H column within 30 au using the kinematic information in the line profile. This is discussed in Appendix A. The shown upper limits in Figure 1 assume a column of C_2H that is constant in the inner 20 (AS 209) or 30 (HD 163296 and MWC 480) au.

We adopt the CO-depletion factor Zhang et al. (2021) derived from the observed CO isotopologue radial profiles (Law et al. 2021a). Zhang et al. (2021) built disk-specific models based on high-resolution continuum and CO isotopologue (^{13}CO and $C^{18}O$) line data. A total gas-to-dust mass ratio of 100 is assumed, with the gas disk size set by the extent of CO isotopologue emission. Gas and small dust (0.005–1 μm) are well coupled and have the standard tapered power-law surface density distribution and a vertical Gaussian density distribution (see Zhang et al. 2021, for the disk parameters). The large dust is settled at 0.2 times the gas scale height and structured to match the observed millimeter structure (see Tables 1 and 2 and Figure 5 in Zhang et al. 2021). The CO abundance in the disk is then varied until the model CO isotopologue line emission matches the observed line emission for ^{13}CO and $C^{18}O$ for both the $J = 2$–1 and $J = 1$–0

[24] http://www.alma-maps.info

[25] We note that nitrogen abundance can also be indicative of a planet's origin (Cridland et al. 2017), and that it is possible to constrain the nitrogen abundance within protoplanetary disks (Cleeves et al. 2018), which will be the subject of future work.

[26] All planet masses assume a viscous α (Shakura & Sunyaev 1973) of 10^{-3}.

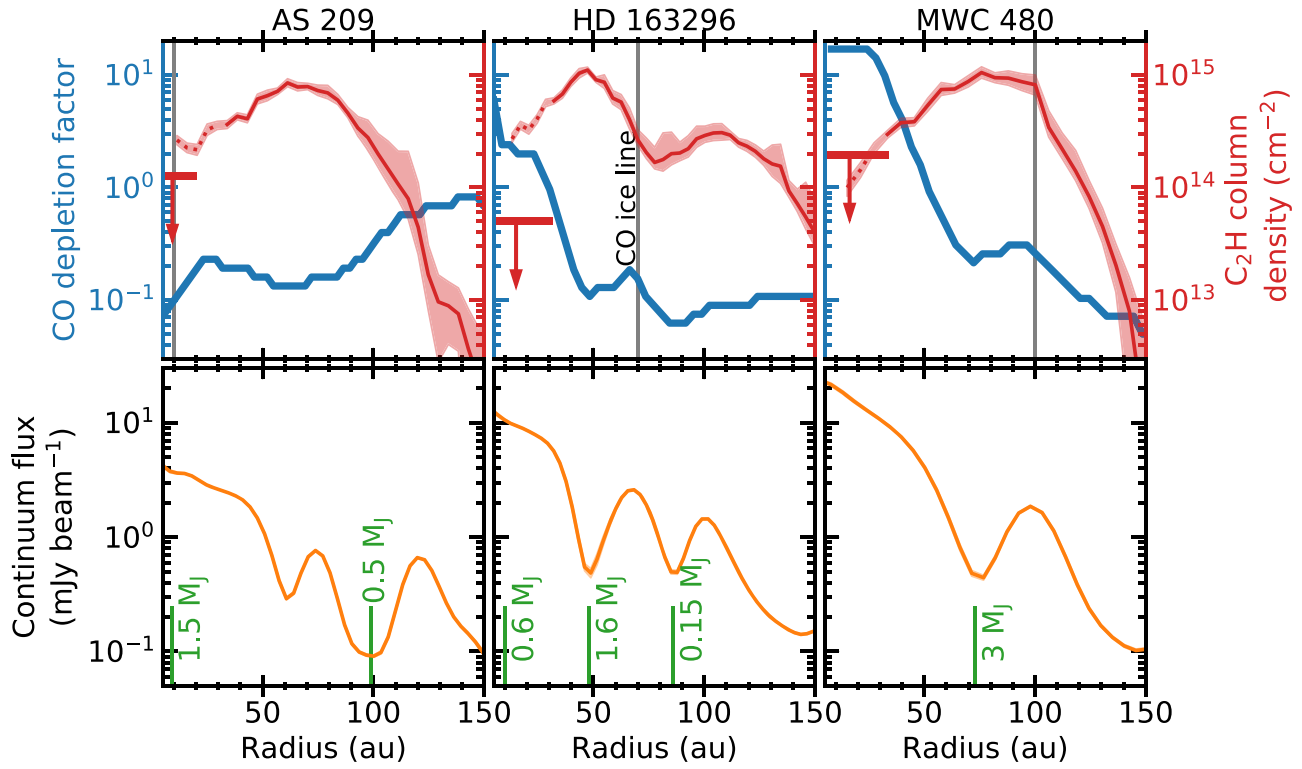

Figure 1. Top: comparison of the CO depletion (blue, left axis) from Zhang et al. (2021) with the C_2H column (red, right axis) derived in Guzmán et al. (2021) for (from left to right) the AS 209, HD 163296, and MWC 480 disks. The solid line shows where the C_2H column density derivation is assumed to be robust. In the inner 30 au, the image cube–based fitting technique is less robust, and the column density–derived values for these radii are shown with a dotted line. For each disk, the upper limit to the C_2H abundance in the inner disk as derived from the line profiles is also shown (see Appendix A). The gray vertical line shows the location of the CO ice line. Bottom: continuum azimuthal average radial intensity profile from Sierra et al. (2021) at 220 GHz. The green vertical lines show the locations of planets inferred from the millimeter dust structure, together with their inferred mass (all planet masses assume a viscous alpha of 10^{-3}; Zhang et al. 2018; Liu et al. 2019).

Table 1
Initial Abundances for the Chemical Models

Species	C/O = 0.47	C/O = 1.0	C/O = 2.0
H_2	0.495	0.495	0.495
H	0.01	0.01	0.01
H_2O[a]	1.53×10^{-4}	10^{-10}	10^{-10}
CO[a]	1.35×10^{-4}	1.35×10^{-4}	1.35×10^{-4}
CH_4[a]	10^{-10}	10^{-10}	1.35×10^{-4}
N_2	1.07×10^{-5}	1.07×10^{-5}	1.07×10^{-5}
S	1.91×10^{-8}	1.91×10^{-8}	1.91×10^{-8}
Si	7.94×10^{-8}	7.94×10^{-8}	7.94×10^{-8}
Fe	4.27×10^{-9}	4.27×10^{-9}	4.27×10^{-9}
Mg	1.00×10^{-11}	1.00×10^{-11}	1.00×10^{-11}

Note.
[a] The H_2O, CO, and CH_4 abundances shown here assume a CO-depletion factor of 1.0. The actual abundance of these species at each radius is obtained by multiplying these abundances by the CO-depletion factor of Figure 1.

transitions. The ratio between the abundance necessary to reproduce that data and the ISM CO abundance is called the CO-depletion factor. The model CO columns are consistent with the CO column derived from the hyperfine lines of $C^{17}O$ in the regions where the latter is detected. Both the C_2H column and the CO-depletion factor are shown in Figure 1.

2.2. C_2H Chemistry

The chemistry of C_2H and its use as a tracer of the elemental C/O ratio in protoplanetary disks has been discussed for a variety of sources and conditions (e.g., Jansen et al. 1995; Nagy et al. 2015; Bergin et al. 2016; Cleeves et al. 2018; Bosman et al. 2021). As a radical, it is most abundant in regions with an active photochemistry, where it is continuously produced and destroyed. The chemistry of C_2H is tightly linked to that of CH_4 and C_2H_2, which is the main reservoir of carbon that is not locked in CO. The C_2H can be directly formed by photodissociation of C_2H_2, or it is formed by dissociative recombination of the $C_2H_2^+$ and $C_2H_3^+$ ions, which are part of a gas-phase hydrocarbon radical and ion cycle (see, for example, Figure 1 of Bosman et al. 2021).

Table 2
Temperatures Used for the C_2H Column Derivation

Source	Gas Temperature (K)	Dust Emission Temperature (K)
AS 209	30.2	12.4
HD 163296	53.8	22.7
MWC 480	69.1	25.5

The C_2H abundance is very dependent on the C/O ratio in the gas, with reactions such as $C_2H + O \rightarrow CO + CH$ and $CH + O \rightarrow CO + H$ directly driving down the C_2H abundance, as well as removing carbon from the hydrocarbon reservoir. Reactions generally result in the formation of CO, which is stable against photodissociation (van Dishoeck & Black 1988). As such, this carbon is no longer available for hydrocarbon chemistry. Depending on the physical structure of the disk and the stellar radiation field, the C_2H column density in a disk model can vary by 4 orders of magnitude just by variations of the C/O ratio between ~0.5 and 2.0 (Bergin et al. 2016;

Cleeves et al. 2018). This makes C_2H a very good tracer of the C/O ratio.

As a radical, C_2H traces the photodissociation region (PDR) layers of the disk. At low C/O ratios, all carbon for C_2H comes from the dissociation of CO, which happens only in the top layer of the disk PDR, where CO self-shielding is not yet active. The mass in this thin layer is relatively constant in a disk, as well as disk to disk, as it depends on a fundamental property of the CO molecule, which starts to self-shield at a column of 10^{15} cm^{-2} (van Dishoeck & Black 1988). At C/O ratios above 1, the carbon for the formation of C_2H can be extracted from hydrocarbons such as CH_4 and C_2H_2. The thickness of the layer in which these hydrocarbons can be dissociated depends on UV attenuation by dust. The small-dust content of the disk atmosphere thus has an effect on the measured C_2H column. Initial calculations in Bosman et al. (2021) predict that the small-dust content will impact the C_2H abundance but is relatively weak. An order-of-magnitude drop in the small-dust abundance should only lead to an increase in the C_2H abundance by a factor of 2.

2.3. Modeling Setup

In our modeling, we start with the model structure and CO-depletion factor as derived by Zhang et al. (2021). We vary the C/O ratio and the amount of small dust in the surface layers, as these parameters have the most impact of the C_2H abundance. The small-dust content of the disks is varied by multiplying the small-dust abundances by a constant factor of 0.001, 0.01, 0.1, or 1 from the base models of Zhang et al. (2021). The last of these are the fiducial dust structures and are identical to those used in Zhang et al. (2021).[27] Each model has a constant C/O ratio of either 0.47, 1.0, or 2.0. These correspond to the volatile ISM level (0.47), CO-dominated gas (1.0), and a high C/O value (2.0). Increasing the C/O ratio above 2.0 no longer has an impact on the C_2H abundance (e.g., Cleeves et al. 2018). Combining the four different small-dust abundances and three different C/O ratios, this results in 12 models per disk studied.

The model calculation is done in two steps. In the first step, the dust and gas temperatures are calculated. We start from the best-fit structure and CO-depletion factors from Zhang et al. (2021). The structures are here modified to vary the small-dust content. The abundances of H_2O and CH_4 in the initial conditions of the chemical network are also modified at this point, so the gas temperature calculation includes the changes in composition driven by the different C/O ratios. The dust and gas temperatures are then calculated using DALI with the standard reduced chemical network, which correctly calculates the abundances of the major gas coolants (Bruderer et al. 2012; Bruderer 2013). In the second step, a full gas-grain network was used to calculate the 2D chemical composition based on the physical conditions determined in the first step.

This two-step approach was chosen to balance consistency with feasibility. To calculate the gas temperature, the chemical solver has to run multiple times per cell, which is prohibitively expensive to do with the gas-grain chemical network. As mentioned, this approach does capture the effects of the C/O ratio on the gas temperature, and the effect of these changes on the resulting chemistry, while being computationally tractable.

[27] For models with lower small-grain abundances, the model SED no longer fits the observational SED.

2.4. Gas-grain Chemical Network

The gas-grain chemical network used for the second step of our calculations is based on the network of Walsh et al. (2015), which is a combination of the UMIST12[28] (McElroy et al. 2013) for the gas-phase reactions and the Ohio State University network (Garrod et al. 2008) for the grain surface reactions. Molecular binding energies are from McElroy et al. (2013) and Penteado et al. (2017), with small adjustments for NH_x and CH_x radicals (Bosman et al. 2018). These binding energies are tabulated in Bosman et al. (2018, Table B.2). The freeze-out of H_2 is also treated as in Bosman et al. (2018), using the higher (430 K) binding energy for H_2 when there are less than two layers of H_2 ice but lowering the binding energy to 100 K when H_2 covers the ice completely.

Photodesorption yields are taken from experiments where available (Öberg et al. 2009a, 2009b, 2009c) and assumed to be 10^{-3} otherwise. All photodesorption is assumed to yield intact molecules in the gas phase.[29] The grain surface chemistry assumes a diffusion-to-binding energy ratio of 0.3 and a tunneling barrier of 1 Å (as in Bosman et al. 2018). For photodissociation, the wavelength-dependent cross sections of Heays et al. (2017) are used in combination with the wavelength-dependent UV field that DALI calculates. For the few cases in which Heays et al. (2017) did not have a compilation of the wavelength-dependent cross sections, the rate parameterization of McElroy et al. (2013) is used. Self-shielding and mutual shielding is included for C, CO, N_2, and H_2 (Draine & Bertoldi 1996; Kamp & Bertoldi 2000; Visser et al. 2009, 2018).

The initial abundances used in the models with different C/O ratios are tabulated in Table 1. Any molecule, atom, or ion not listed in the table has zero abundance at the beginning of the chemical calculation. The abundances of H_2O, CO, and CH_4, that is, the initial carbon and oxygen carriers, are scaled with the CO-depletion factors derived in Zhang et al. (2021; see Figure 1). Further, the abundances have been chosen such that for the maximum amount of CO that can be formed, that is the lowest of the carbon and oxygen elemental abundances, is the same for all three of the C/O ratios. CH_4 was chosen as the carrier for the excess carbon (instead of elemental C) in the models. The exact initial abundances do not matter greatly for this calculation, as abundances in the C_2H layer will be set by photon-dominated steady-state chemistry (Bosman et al. 2021). The only exceptions to this rule are the large (more than seven carbon atoms) carbon chains, which act as refractories in the intermediate PDR layers. These large carbon chains are only formed in the models when a significant fraction (>10%) of the carbon is in elemental or ionized form. To prevent this, an elemental or ionized form should not be chosen for the initial carbon carrier. In other cases, the exact carrier of the excess carbon does not substantially alter the resulting C_2H abundance (Bosman et al. 2021).

A low cosmic-ray ionization rate of 10^{-18} s^{-1} is used for the chemical models, similar to the models in Zhang et al. (2021; see, e.g., Cleeves et al. 2013, for a discussion of cosmic-ray propagation in disks.). A higher cosmic-ray ionization rate, coupled with the already low CO abundances currently assumed, would quickly convert the remaining CO into other species, like CH_4, CO_2, and

[28] http://udfa.ajmarkwick.net/

[29] Many molecules are expected to fragment on absorption of a UV photon, with some of the fragments released from the ice instead of photodesorbing intact as assumed. Fragmentation has been shown for methanol (Bertin et al. 2016) and is expected for other, larger molecules. This is not expected to impact the chemistry of the species studied here.

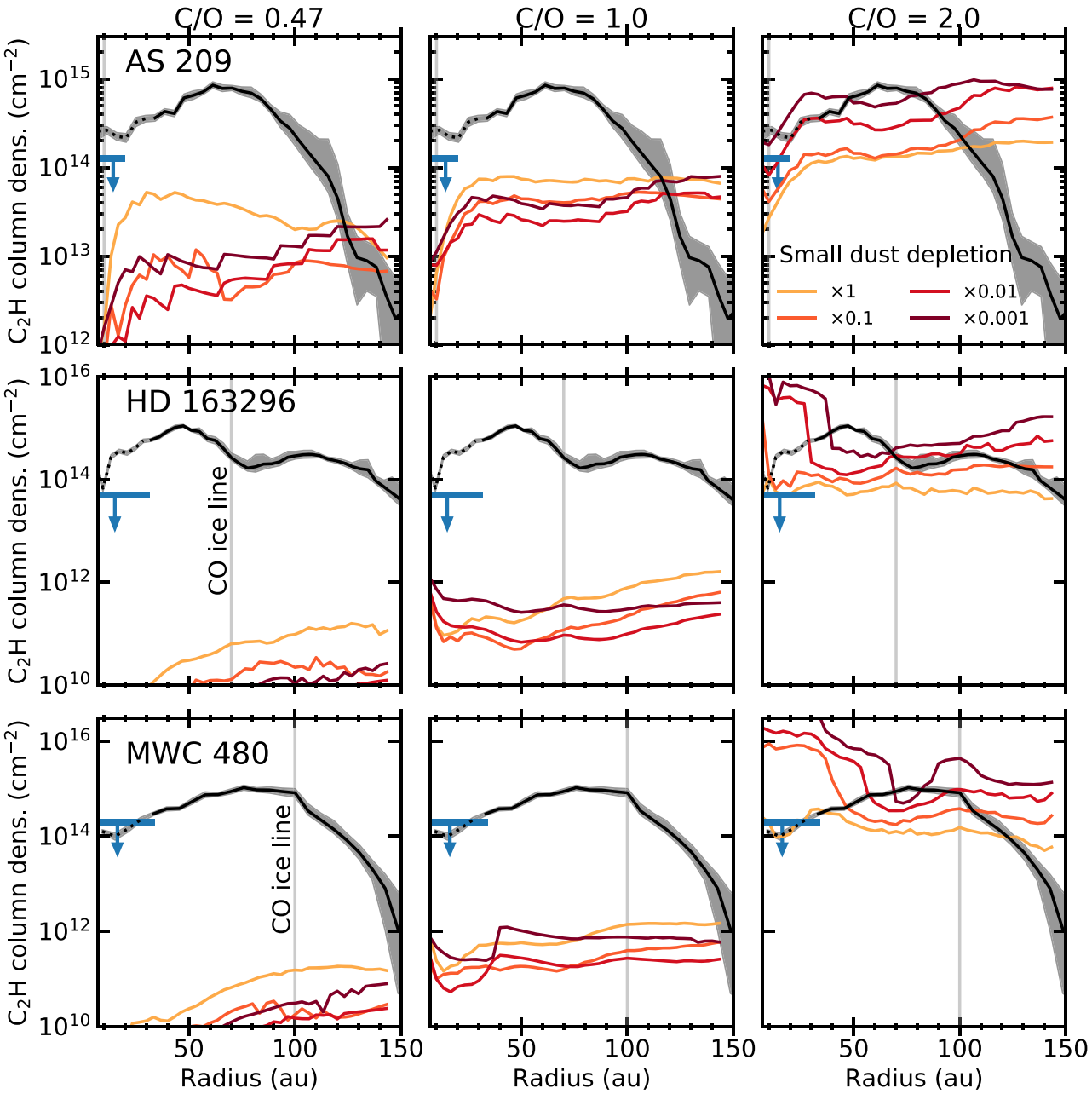

Figure 2. The C_2H column densities as function of radius for AS 209 (top), HD 163296 (middle), and MWC 480 (bottom). From left to right, the figures show models with C/O ratios of 0.47, 1.0, and 2.0, with the colors showing the depletion of the small-dust grains from the fiducial value (yellow) to 1000× depleted (dark red). The black line with the gray error region shows the column densities extracted from the data (Guzmán et al. 2021); the black line transitions into a dotted line in the harder-to-probe inner 30 au. The blue bars and arrows show the inner disk C_2H column density upper limits derived from the line profiles (see Appendix A). The vertical gray line shows the location of the CO ice line in the models. The model C_2H column densities are integrated over both sides of the disk. High C/O ratios are necessary to reproduce the observed C_2H column densities.

CH_3OH (e.g., Furuya & Aikawa 2014; Schwarz et al. 2016; Bosman et al. 2018), in the 1 Myr chemical timescale that is assumed. This would create a disagreement between the CO column in the models and the intended, observationally motivated CO column density. This cosmic-ray ionization rate is thus not the rate necessary to lower the CO abundance from the ISM level to the observed levels, but it is the cosmic-ray ionization rate that has to be used to prevent the CO abundance from dropping further. We note that the cosmic-ray ionization rate used does not impact the C_2H abundance in chemical models (Cleeves et al. 2018) and that the cosmic-ray ionization rate used here is consistent with modeling of MAPS sources by Aikawa et al. (2021).

Appendix B shows the CO columns for difference C/O ratios for the three disks compared to the CO columns derived from the data. The difference C/O ratios do not impact the CO column in the model. Furthermore, the agreement between our model CO columns and the results from Zhang et al. (2021) indicate that the amount of volatiles in the surface layer is representative of the disks studied.

3. Composition of the Disk Gas

Figure 2 shows the model and observed C_2H column densities for the AS 209, HD 163296, and MWC 480 disks for

C/O ratios of 0.47, 1.0, and 2.0 and the different depletion factors for the small-dust grains. The 2D C_2H abundance structures can be found in Appendix C, together with a discussion of the chemical behavior of the C_2H. As expected, the C/O ratio has a large effect on the C_2H column density, especially the jump from C/O = 1.0 to 2.0.

Figure 2 clearly shows that C/O ratios $\geqslant$2.0 are necessary to match the high, $>10^{13}$ cm^{-2}, C_2H column densities observed in the inner 100–150 au of the AS 209, MWC 480, and HD 163296 disks. A high C/O ratio, $\geqslant$2.0, has difficulty reproducing a C_2H column density above 10^{14} cm^{-2} in the fiducial small-dust model. In each model, all but the peak of the C_2H column density can be reproduced by a factor of 1000 or less of small-dust depletion. The difference between the C_2H column in the 1000 times depleted small-dust model and the observed column peak are below a factor of 2. Maxima in the derived C_2H column have some colocality with the first deep gap in the millimeter disk and region of low CO abundance (Figure 1; Guzmán et al. 2021; Law et al. 2021a; Zhang et al. 2021). However, peaks in the C_2H emission (and column) are much broader than the gaps seen in the millimeter disk. Interestingly, the secondary peak around ∼110 au in the HD 163296 C_2H abundance structure does not line up with the second strong dust gap around ∼85 au. This is further explored in Section 4.2.

The C_2H column density drops sharply toward large radii (>100, >150, and >125 au for AS 209, HD 163296, and MWC 480, respectively). A constant C/O ratio model does not share this abundance drop at this radius, implying that the C/O ratio drops around these radii in these disks.

All three disks show a decrease in the C_2H column density inward of 50 au. All of the AS 209 disk models show a dip in the C_2H column in this region driven by the decreasing CO and thus available carbon abundance in the models. In HD 163296 and MWC 480, the C_2H column density decreases in the region where the CO abundance and thus available carbon content increases. This implies a drop in the C/O ratio in the inner regions of these disks. While this drop is expected to happen at the CO ice line, it appears to happen at a smaller radius for both the HD 163296 and MWC 480 disks. This is discussed in more detail in Section 4.3.

In summary, a high C/O ratio, together with a strong depletion of small dust, is necessary to match maxima in the derived C_2H column. A model with a constant C/O ratio and small-grain depletion is not able to match the full behavior of the C_2H column density radial profiles. Radial variations in the C/O ratio and small-dust content of the disk atmosphere are necessary to reproduce this behavior. The implications of this inference are discussed in Sections 4.2 and 4.3, and for the AS 209 disk, this is studied in more detail in Alarcón et al. (2021).

4. Discussion

4.1. C/O Ratios from C_2H in the Literature

The inferred C/O ratios associated with C_2H emission locations in these disks are 2.0 or higher above most of the millimeter disk. This is higher than previously derived for other disks. Miotello et al. (2019) found that a global C/O ratio of 1.5 reproduced the flux for the sample of Lupus disks studied, significantly lower than the C/O ratios found for these disks. This discrepancy is caused by the fact that the MAPS data resolve the disk emission and reveal existing emission structure. In the gas with strong C_2H emission, a C/O ratio $\geqslant$2.0 is necessary. However, the C_2H column density is not elevated ($>10^{14}$ cm^{-2}) over the entire disk. Thus, in models using disk-integrated flux, a lower, global C/O ratio will be estimated. This will be especially prominent for the three disks studied here, as the C_2H column densities drop below 10^{12} cm^{-2} around 150 au (see Guzmán et al. 2021), which implies C/O ratios <1 for the majority of the disk area.

In the IM Lup disk, the C/O ratio was determined by Cleeves et al. (2018) to be around 0.8, even lower than the C/O ratios found for most of the disk in Miotello et al. (2019). When comparing the C_2H radial profiles in Law et al. (2021a) and C_2H column densities in Guzmán et al. (2021) between the IM Lup disk and the AS 209, MWC 480, and HD 163296 disks, it is clear that the IM Lup disk has less C_2H than the other disks by more than an order of magnitude. The observationally derived C_2H column density for the IM Lup disk is $\sim10^{13}$ cm^{-2} between 70 and 230 au, which is of the same order as the AS 209 disk model column densities for a C/O of 0.47 and 1.0. The elemental composition of the IM Lup disk is thus clearly different from the three disks studied here.

The difference between the composition of the IM Lup disk and the other disks studied here could be due to the young age of the IM Lup disk (Mawet et al. 2012). The process responsible for turning the volatile rich and oxygen-dominated ISM composition gas into the volatile poor and carbon-rich gas seen in many other disks could then still be underway (Bergner et al. 2020; Zhang et al. 2020b). This composition transition can be the result of either more efficient trapping of oxygen-carrying species, e.g., water, CO, and CO_2, as ices coating millimeter-sized dust particles that are confined to the midplane (Krijt et al. 2020) or the release of carbon from a refractory source in a uniformly depleted surface layer (Bosman et al. 2021). Alternatively, the IM Lup disk has less pronounced substructures in the millimeter disk. This could simply be a result of the young age, but it can also imply that these substructures are, at least partly, responsible for the high C/O ratios (Bergin et al. 2016; Bosman et al. 2021).

4.2. Structure in the C_2H Column Density

While it is clear that to match the high ($>10^{13}$ cm^{-2}) column densities of C_2H in the AS 209, MWC 480, and HD 163296 disks, C/O $\geqslant$ 2 is necessary, it is not obvious what causes the radial structures in the C_2H column density. These can be caused by either a variation of C/O ratio when the C/O ratio is below 2.0, a variation in small-dust content when the C/O ratio is larger than unity, or a combination of both. The effects on the C_2H column density due to changes in the C/O ratio are generally larger than those due to changes in the small-dust content (Figure 2).

The regions in which a depletion of small grains must be invoked to match the C_2H column density is wider than the millimeter dust gaps seen in these three disks. As the chemical timescales are short, <1000 yr (Bosman et al. 2021), diffusive spreading of C_2H from the millimeter gap, which happens on timescales $>10^4$ yr, can be ruled out. This is thus suggestive of a wider small-grain gap, around the millimeter dust gap, possibly due to the millimeter dust rings acting as a small-grain sink in a manner similar to that predicted from the midplane (Krijt & Ciesla 2016).

In the HD 163296 disk, the C_2H column density outside 70 au is consistent with an elevated C/O ratio of 2.0 and factor of ∼10 of small-dust depletion. At 50 au, the radius of a

prominent gap in the millimeter continuum, the C_2H column density is more comparable to the small-grain model with a factor 100 depletion. This indicates that the UV penetrates deeper into the disk around the millimeter dust gap. This is not seen in the second dust gap at 90 au, where there is a local minimum in the C_2H abundance. A possible explanation for the difference in C_2H column density can be found in the scattered-light image. There is a bright ring in scattered light associated with the 66 au submillimeter dust ring (e.g., Garufi et al. 2014; Monnier et al. 2017; Muro-Arena et al. 2018). This ring of abundant small dust could shadow the region of the second dust gap, lowering the available UV flux in the gap and thus lowering the C_2H column density.

The C_2H column density in the MWC 480 disk peaks around 70 au, the location of the millimeter continuum dust gap (Liu et al. 2019; Long et al. 2019; Law et al. 2021a). Similar to the gap at 50 au in the HD 163296 disk, high UV penetration at the gap location—again suggestive of small-grain depletion—is necessary.

The need for additional small dust depletion on top of the fiducial dust models that already have a degree of dust depletion in the surface layers implies gas-to-dust ratios in the surface layers of at least 10,000 and up to 10^6 at the location of the C_2H emission peak in the AS 209 disk (Zhang et al. 2021). It is thus possible that other processes are increasing the C_2H abundance above the levels predicted by the chemical models. One intriguing possibility is that strong vertical or radial mixing is operating, which could cycle C_2H_2 and other larger carbon species from more shielded regions into the 25–75 au region. This would lead to an out-of-equilibrium chemistry with a higher C_2H abundance. This could be consistent with a large-scale meridional flow into the gaps and would be an interesting subject of further study.

4.3. A Link between CO Abundance and C/O

It has been suggested that a low CO abundance and a high C/O ratio have a common dynamical or chemical origin, which should cause a correlation between CO abundance and C/O ratio (Bergin et al. 2016). However, a relation between C_2H flux and CO abundances, as traced by ^{13}CO over millimeter dust flux, has not been found (Miotello et al. 2019). The relation has not been studied as a function of radius in a disk, where, for example, the release of CO at the CO ice line is expected to have a strong impact on the gas-phase C/O ratio (Öberg et al. 2011).

For the MWC 480 and HD 163296 disks, the regions within and outside of the CO ice line are resolved by the observations. The emission maps of $C^{18}O$ (and the derived CO column) do not exhibit a strong response at the CO ice line location predicted by the detailed disk physical models. Most directly, the CO abundance at the CO ice line does not return to the ISM level (e.g., 10^{-4} relative to H_2; Zhang et al. 2021, Figure 1). This is consistent with a lack of the expected C_2H column density drop at the CO ice line. Without the return of CO, the C/O ratio does not drop toward unity but stays high. Closer to the star, there is an increase in the CO abundance, reaching greater-than-ISM levels at 50 au in MWC 480 and 30 au in HD 163296.

The increase in CO abundance at these radii is accompanied by a drop in C_2H column density (see Figure 1) consistent with a drop in C/O ratio (Figure 2) due to the return of the oxygen carried by CO into the gas. As mentioned, the location of the CO abundance rises is not where the CO ice line is expected, based on the thermal structure in the models (Calahan et al. 2021; Zhang et al. 2021). Temperatures in the region where the CO abundance rises are between 25 and 30 K in the standard MAPS models (Zhang et al. 2021). These temperatures are in line with modeling by Calahan et al. (2021) for HD 163296 and empirical temperature measurements from the CO isotopologue emission (Law et al. 2021b). Furthermore the location where the C_2H column drops below the $C/O = 2$ models is at smaller radii than the rise in CO abundance. This implies that when the CO abundance rises to close to the ISM value, the C/O ratio drops.

If the rise of the CO abundance is due to CO coming off the grains, this would imply a higher binding energy than the 850 K (∼22 K ice line temperature; e.g., Harsono et al. 2015) assumed in the models, or could be due to a different physical process. One possibility is large, icy grains drifting across the CO ice line, but only depositing the CO into the gas at a radius well within the CO ice line location. The exact effects are going to be very disk-dependent. A higher CO desorption temperature was also inferred for CO in TW Hya (Zhang et al. 2017). This could be indicative for CO as desorbed on an H_2O or CO_2 mixture (Noble et al. 2012; He & Vidali 2014). In the case of HD 163296 and MWC 480, in which the CO content of the grains is expected to be high, this would indicate that the vast majority of the ∼100 monolayers of CO are all in high binding energy sites. Moving the ice line by ∼40 au requires fast radial drift. Only grains between 1 and 10 cm reach the right drift and desorption speeds (Piso et al. 2015). This is larger than the 3 mm grains that Sierra et al. (2021) needed at these radii to fit the multiband continuum data.

A similar relation between CO and C_2H abundance is seen in the outer disk of AS 209, where outside 100 au, the CO abundance increases and the C_2H column density drops, again implying a low C/O ratio when the CO abundance is high. The HD 163296 and MWC 480 disks also show a drop in C_2H column density and inferred C/O ratio outside ∼120 and ∼150 au, respectively. This is not paired with an increase in CO abundance, however. This implies that a high C/O ratio happens only in the regions with low CO abundance. However, something in addition to low CO abundance is needed to explain a high C/O ratio. This could be related to the presence of an additional carbon source, such as the photoablation of carbonaceous grains (Bosman et al. 2021).

4.4. Composition of Planet-building Material

To properly predict the composition of a planet forming at a certain location, it is necessary to know the elemental composition of the building materials. For any planet forming outside of 30 au in the AS 209, HD 163296, and MWC 480 disks, such as those inferred in the various gaps in these systems, it is now possible to make some inferences on the composition of the gas and solids that will go into these putative planets. For this discussion, we will assume that the bulk of the gas mass is accreted late in the disk lifetime, such that the composition of the disk gas inferred here is representative of the gas accreted onto the planet. If planets accrete their gas mass early in the disk lifetime, when accretion onto the disk still delivers significant pristine material, planetary composition will be very similar to that of the host star.

The C_2H emission in these three disks is strong, but an emission surface height cannot be derived unambiguously over the entire disk (Law 2021b). This implies either that the line is optically thin, and thus too weak to measure a height, or that it comes from below the ^{13}CO surface, which results in a measured height that is consistent with the disk midplane. The hyperfine ratios, from which the C_2H column densities have been derived, show that the lines are optically thick. This means that the C_2H lines come from deeper than the ^{13}CO emission. This is consistent with the disk regions where the C_2H height can be derived (Law 2021b) and in agreement with the models that have most of their column density between one and two scale heights (see Appendix C; the scale heights in these disks at 10–200 au vary between z/r of 0.06 and 0.1, depending on the disk; Zhang et al. 2021). At this height, mixing with the midplane is efficient and happens on 10 kyr timescales for turbulent viscosity coefficients of $\alpha \approx 10^{-3}$ (Ciesla 2010). As such, it is unlikely that strong vertical elemental abundance gradients exist, so the high C/O abundances and low O/H abundances necessary to explain the C_2H emission likely hold for the disk midplane as well. Furthermore, if accretion onto a planet happens through meridional flows, the gas accretion onto the planet will actually sample the vertical height from where the C_2H emission originates (Tanigawa et al. 2012; Morbidelli et al. 2014); such flows have been observed in the higher layers of the disk with ^{12}CO in the HD 163296 disk by Teague et al. (2019). As these are the flows that feed the planet, gas from the C_2H-emitting layer is expected to contribute significantly to the planetary accretion after gap opening (Morbidelli et al. 2014; Cridland et al. 2020).

The number of small grains in the disk atmosphere that can accrete with the gas onto the planet is strongly reduced from the ISM level of 1% of the total mass. This happens both globally, in the disk surface due to grain growth and settling, and locally, as the inferred C_2H column densities necessitate more UV penetration in certain disk locations. The combined low CO abundance and depleted small dust thus implies that most of the ISM carbon and oxygen, both volatile and refractory, is not present in gas accreting onto planets that have reached pebble isolation mass.

Gas giants that accrete most of their atmospheres after reaching the pebble isolation mass thus obtain envelopes, with substellar C/H and O/H and high ($\gg$1.0) C/O ratio compositions, unless efficient release of volatiles from the core or late enrichment by planetesimals takes place. These potential planets are formed at large radii, where CO can be depleted efficiently (>50 au radii for HD 163296 and MWC 480). If these planets do not migrate from their formation location, they are prime targets for composition analysis by direct imaging with the James Webb Space Telescope, the most notable example being the planets in the HR 8799 system. Substellar carbon and oxygen abundances and a high C/O composition would distinguish planets formed through pebble or core accretion from planets formed as a result of a gravitational instability. The latter are expected to have stellar or superstellar C/H and O/H ratios with a stellar or substellar C/O ratio (e.g., Ilee et al. 2017).

Compositions of planets at large radii so far do not show the signature predicted from the disk observations. The planet β Pic b has a low derived C/O ratio, which is expected to be close to or below the stellar C/O ratio (Gravity Collaboration et al. 2020). This rules out a formation scenario in which one of the >40 au putative planets in the disks studied here migrates inward to 9 au (Lagrange et al. 2020), unless this planet accreted >40 $M_\oplus$ of oxygen-rich ice or mixed a similar amount of ice from the core into the atmosphere (Gravity Collaboration et al. 2020). Three other large-radius (>50 au) planets have their water abundance measured (κ And b, HR 8799 b, and HR 8799 c; Todorov et al. 2016; Lavie et al. 2017; Madhusudhan 2019). The water abundances are higher than the disk atmosphere gas, ice, and refractory oxygen abundances combined by a factor of 2–100 for the three disks studied here. If these planets are the successors of the putative planets in these disks, a significant amount of disk water ice needs to make it into the atmosphere, at least 30 $M_\oplus$ for κ And b and HR 8799 b and around 100 $M_\oplus$ for HR 8799 c (Madhusudhan 2019). This would imply very massive cores (60–200 $M_\oplus$) and very efficient core mixing, 6–20 $M_\oplus$ Myr^{-1} planetesimal accretion rates for a 10 Myr disk age, or a gravitational instability origin from a moderately (factor of 1–3) water ice–enhanced core. The low water abundance measured for many transiting exoplanets is comparable to the low total oxygen abundance in the gas at large (>50 au) radii in the AS 209, HD 163296, and MWC 480 disks (Madhusudhan 2019; Welbanks et al. 2019). This could point to an outer disk origin for these hot Jupiters; however, without constraints on the C/O ratio, this remains speculation. A high C/O $\gtrsim$ 1.0 would strengthen the case for an outer disk origin for hot Jupiters.

5. Conclusions

We have studied the behavior of the C_2H column densities above the millimeter pebble disks orbiting AS 209, MWC 480, and HD 163296 and compared them to C_2H column densities to source the specific thermochemical models calculated using DALI (Bruderer et al. 2012; Bruderer 2013) with an extended gas-grain chemical network. We find that high (~2.0) C/O ratios are necessary to explain the strong C_2H emission. The high column densities (>10^{15} cm^{-2}) imply that there is an additional effect at play. One option is more efficient UV penetration, leading to even higher C_2H column densities. The high but localized C_2H column densities explain why these resolved observations need locally higher C/O ratios than global models, like those from Miotello et al. (2019).

Furthermore, a relation between the C/O ratio and CO abundance appears to exist, with a higher CO abundance leading to a lower C/O ratio. This is especially the case when looking at the inner 100 au of the HD 163296 and MWC 480 disks. The transition to an enhanced CO abundance and diminished C/O ratios seems not to happen at the CO ice line, but further in.

The C/O and gas-to-dust ratios are elevated above the stellar and ISM levels (respectively) along the radial extent of the pebbled disk, except in the regions where the CO abundance is high (inner ~30 au for HD 163296 and MWC 480). This includes the regions where most of the dust gaps are located. The gas accreting onto the possibly forming planets is thus strongly depleted of volatile and refractory carbon and oxygen, with a strongly superstellar C/O ratio. In the absence of core–envelope mixing and envelope enrichment by planetesimal collisions, this would lead to a high C/O but generally volatile-depleted giant planets. Comparing this prediction to the composition of gas giants at large orbits, such as will be

inferred by the James Webb Space Telescope, will be able to point to the origin of these large-orbit planets.

This paper makes use of the following ALMA data: ADS/JAO.ALMA#2018.1.01055.L. ALMA is a partnership of ESO (representing its member states), NSF (USA) and NINS (Japan), together with NRC (Canada), MOST and ASIAA (Taiwan), and KASI (Republic of Korea), in cooperation with the Republic of Chile. The Joint ALMA Observatory is operated by ESO, AUI/NRAO and NAOJ. The National Radio Astronomy Observatory is a facility of the National Science Foundation operated under cooperative agreement by Associated Universities, Inc.

A.D.B., F.A., E.A.B., and K.I.Ö. acknowledge support from NSF AAG grant No. 1907653. K.Z. acknowledges the support of the Office of the Vice Chancellor for Research and Graduate Education at the University of Wisconsin–Madison with funding from the Wisconsin Alumni Research Foundation. K.Z., J.B.B., I.C., J.H., and K.R.S. acknowledge support from NASA through NASA Hubble Fellowship grant Nos. HST-HF2-51401.001, HST-HF2-51429.001-A, HST-HF2-51405.001-A, HST-HF2-51460.001-A, and HST-HF2-51419.001 awarded by the Space Telescope Science Institute, which is operated by the Association of Universities for Research in Astronomy, Inc., for NASA, under contract NAS5-26555. M.L.R.H. acknowledges support from the Michigan Society of Fellows. K.I.Ö. acknowledges support from the Simons Foundation (SCOL No. 321183). V.V.G. acknowledges support from FONDECYT Iniciación 11180904 and ANID project Basal AFB-170002. C.W. acknowledges financial support from the University of Leeds, STFC, and UKRI (grant Nos. ST/R000549/1, ST/T000287/1, MR/T040726/1) Y.A. acknowledges support by NAOJ ALMA Scientific Research grant code 2019-13B and Grant-in-Aid for Scientific Research 18H05222 and 20H05847. S.M.A. and J.H. acknowledge funding support from the National Aeronautics and Space Administration under grant No. 17-XRP17 2-0012 issued through the Exoplanets Research Program. A.S.B acknowledges the studentship funded by the Science and Technology Facilities Council of the United Kingdom (STFC). G.C. is supported by NAOJ ALMA Scientific Research grant code 2019-13B. L.I.C. gratefully acknowledges support from the David and Lucile Packard Foundation and Johnson & Johnson's WiSTEM2D Program. J.D.I. acknowledges support from the Science and Technology Facilities Council of the United Kingdom (STFC) under ST/T000287/1. C.J.L. acknowledges funding from the National Science Foundation Graduate Research Fellowship under Grant no. DGE1745303. R.L.G. acknowledges support from a CNES fellowship grant. F.L. and R.T. acknowledge support from the Smithsonian Institution as Submillimeter Array (SMA) Fellows. Y.L. acknowledges the financial support by the Natural Science Foundation of China (grant No. 11973090). F.M. acknowledges support from the ANR of France under contract ANR-16-CE31-0013 (Planet-Forming-Disks) and ANR-15-IDEX-02 (through CDP "Origins of Life"). H.N. acknowledges support by NAOJ ALMA Scientific Research grant code 2018-10B and Grant-in-Aid for Scientific Research 18H05441. T.T. is supported by JSPS KAKENHI grant Nos. JP17K14244 and JP20K04017. Y.Y. is supported by IGPEES, WINGS Program, the University of Tokyo.

Software: SciPy (Virtanen et al. 2020), NumPy (Van Der Walt et al. 2011), Matplotlib (Hunter 2007).

Appendix A
C_2H Column in the Inner 30 au

To set limits on the C_2H column from the inner regions of the disk, we use the kinematic information in the C_2H line profile to determine the flux that is actually coming from the inner disk. First, we filter out flux that seems to be emitted from small radii in the image but is instead flux from larger radii, smeared to the inner regions by the beam. To accomplish this, we use the method outlined in Bosman et al. (2021) to extract spectra from the image cube and then transform these inner disk spectra into radial profiles using the kinematical information assuming the disk is in Keplerian rotation. Instead of using both the red- and blueshifted line wings, as done for CO, we only use the uncontaminated line wing for C_2H. Radial profiles are created for the four strong components of the C_2H $N = 3$–2 transition ($J = 7/2$–$5/2$, $F = 4$–3; $J = 7/2$–$5/2$, $F = 3$–2; $J = 5/2$–$3/2$, $F = 3$–2; and $J = 5/2$–$3/2$, $F = 2$–1). The weaker $N = 3$–2, $J = 5/2$–$3/2$, $F = 2$–2 line does not contaminate the spectrum of the nearest strong line. Figure 3 shows the redshifted wing of the $N = 3$–2; $J = 7/2$–$5/2$, $F = 4$–3 transition together with the extracted radial profile and inner region upper limit for AS 209.

To account for the loss of sensitivity by only having one line wing per fit, we increase the radial grid spacing in the radial profile fitting to 10 au. The emission is weak, and within 30 au, we are mostly constrained to estimating upper limits. Only for the

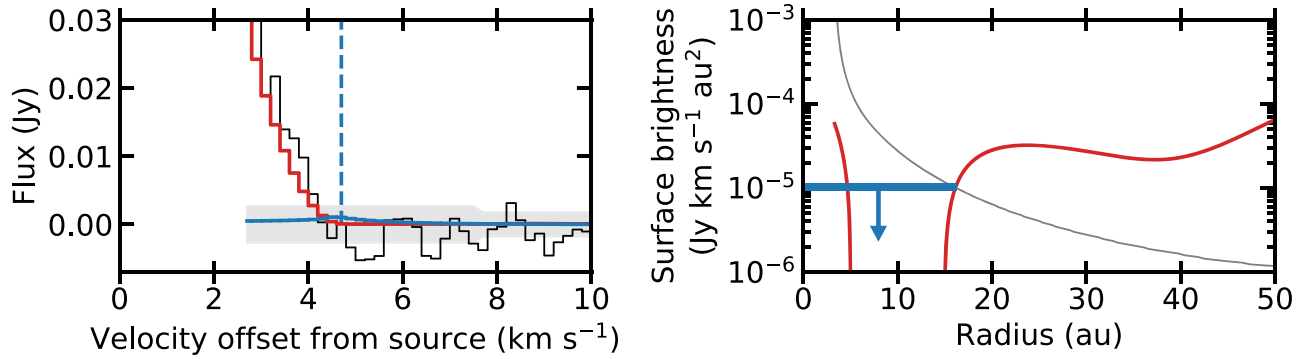

Figure 3. Left: redshifted line wing of the C_2H $N = 3$–2; $J = 7/2$–$5/2$, $F = 4$–3 transition in AS 209 (black). The red line shows a model fit to the flux at >2.6 km s^{-1} from source velocity, corresponding to <55 au for AS 209, and the blue line shows the profile of the flux upper limit in the inner region. Right: fitted radial profile (red) and flux upper limit (blue) derived from the data. The gray line shows the relation between the extent of an emitting area and the minimal, constant flux that would be detectable from that area given the noise in the data. This is our sensitivity limit estimate. The point where the fitted radial profile dips under this sensitivity limit is where we set the flux upper limit for the innermost region.

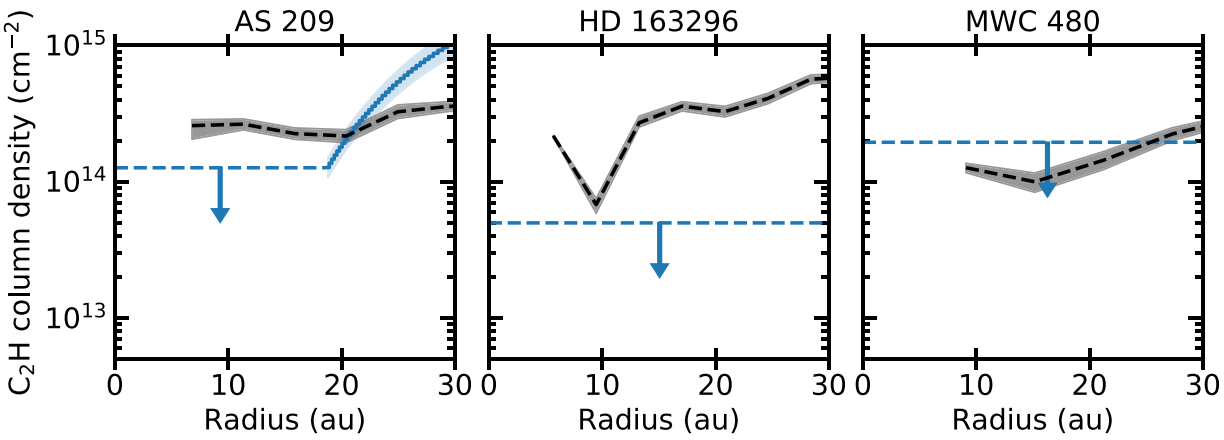

Figure 4. Comparison of the image-derived C_2H column (black; Guzmán et al. 2021) and the column density derived from the line profiles (blue) in the inner 30 au for the AS 209, HD 163296, and MWC 480 disks. The analysis in the image plane is overestimating the C_2H column in the inner disk.

AS 209 disk can some flux be ascribed to the 20–30 au region. The radial extent, as well as the flux upper limit derived, are taken from the radial profiles, and these are converted into a column upper limit for the inner disk. To convert flux into column densities, we follow Bergner et al. (2020), taking the quantum values for C_2H from the JPL database (see Guzmán et al. 2021). To infer a molecular column density from the observed line flux, the gas and continuum emission temperatures are necessary. For the gas temperature, we assume the temperature from Law (2021b) for ^{12}CO $J = 2$–1 at 30 au, and for the continuum, we take the brightness temperature at 30 au from Sierra et al. (2021); using disk center values changes the derived columns by less than a factor of 2. Values are given in Table. 2. We also assume LTE and that the line width is fully thermal. Figure 4 compares the derived limits from the line profiles to the columns derived from the images.

Appendix B
Tracing the Gaseous Volatile Content with CO

Figure 5 compares the CO column densities derived by Zhang et al. (2021) and the CO column densities extracted from the gas-grain network for the three different C/O ratios tested here for the thermochemical models with undepleted small dust. The CO column densities in the DALI models match well for models of the MWC 480 and HD 163296 disks, but the AS 209 DALI models produce higher CO column densities than in the AS 209 RAC2D model.

The AS 209 RAC2D model has a significant amount of carbon in CO_2 ice, while in the DALI models, CO_2 is barely formed, leaving more carbon in gas-phase CO near the midplane. This is due to the more simplified implementation of the grain surface chemistry in RAC2D (Du & Bergin 2014). This difference is only seen in the AS 209 model due to the larger X-ray luminosity and lower UV luminosity in the AS 209 model compared to the HD 163296 and MWC 480 models. In the latter two models, the low X-ray flux and higher UV flux suppress the formation of CO_2 in the RAC2D models, putting them in line with the DALI models.

Lowering the carbon and oxygen abundances in the DALI AS 209 models by a factor of 2–3 within 120 au would lead to a better match of the DALI CO column to the CO column that is used to reproduce the observed emission in the RAC2D models. This drop in carbon and oxygen abundance would only very slightly lower the C_2H abundance and would not impact our conclusions on the C/O ratios of these disks. Therefore, we will continue to use the CO-depletion factors as derived for AS 209 in Zhang et al. (2021).

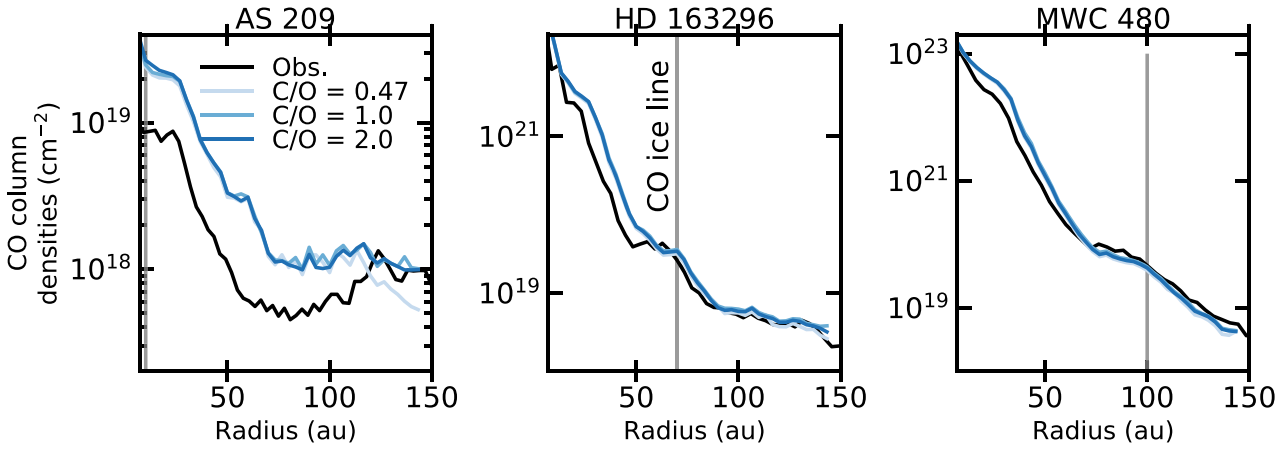

Figure 5. The CO column densities for the fiducial dust models for different C/O ratios (blue) compared to the derived CO column densities from the data (black; Zhang et al. 2021). Vertical gray lines show the CO ice line location extracted from the RAC2D models (Calahan et al. 2021; Zhang et al. 2021).

The small variation between the DALI models with different C/O ratios showcases the chemical stability of CO. In both oxygen- and carbon-rich environments, CO incorporates the vast majority of either the carbon or the oxygen, whatever is in short supply. The CO remains the most abundant observable molecular carrier of elemental C and O. The CO column is thus a good tracer for the gaseous volatile content at a large range of C/O ratios.

Appendix C
C_2H Abundance Structures

Figures 6, 7, and 8 show the C_2H abundance structures for some of the AS 209, HD 163296, and MWC 480 models that feed into the column densities shown in Figure 2. There is a clear difference between the AS 209 disk and the MWC 480 and HD 163296 disks at low C/O ratios, with a higher C_2H abundance in the AS 209 disk. This is driven by different levels of UV and X-ray flux in these sources. The high X-ray flux of AS 209 allows for more efficient destruction of CO, followed by CH_4 and H_2O formation. The lower gas–to–small dust ratio in the surface layer produces less UV penetration, so CH_4 and H_2O are not quickly reverted back to CO; this allows for higher C_2H abundances at low C/O ratios. This also explains why the C_2H column density strongly drops in AS 209 for a C/O ratio of 0.47 when the small dust is depleted, the deeper penetrating UV destroys both CH_4 and H_2O. This increases the amount of atomic oxygen in the gas and lowers the amount of carbon not in CO. The low X-ray flux and larger gas-to-dust ratios in the fiducial HD 163296 and MWC 480 disk models more efficiently force carbon into CO. Only when carbon is more abundant than oxygen does the C_2H production take off.

Changes in the predicted C_2H column densities due to modifications of the small-dust distribution are smaller than the effect of varying the C/O ratio in all three disk models. For $C/O \leqslant 1.0$, the C_2H column density is not strongly dependent on the small-grain column, and no uniform change with a varying small-grain content is seen. At $C/O = 2$, the models with different small-grain abundances in the surface layers clearly follow the small-grain abundance.

This nonlinear interplay between the small-dust abundance and C/O ratios is linked to the carbon source for the C_2H. At $C/O \leqslant 1.0$, the carbon for C_2H needs to be released from CO. As CO efficiently self-shields, the amount of CO that is dissociated does not strongly depend on the continuum UV penetration and is thus not strongly dependent on the small-grain abundance. At high C/O, the carbon comes from CH_4 and other hydrocarbons deeper into the disk. Increasing UV penetration will make it easier to extract carbon from these species and thus increases the C_2H abundance (see Bosman et al. 2021, for a more complete discussion).

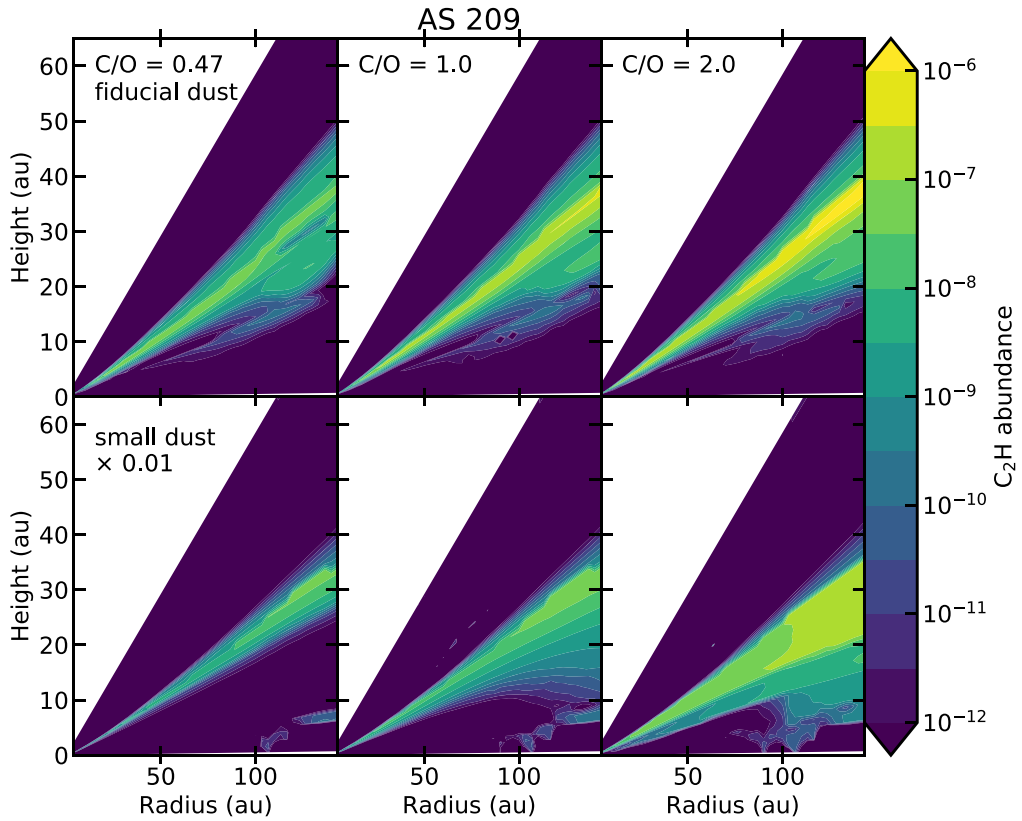

Figure 6. The AS 209 C_2H abundance structure for the fiducial small dust (top) and factor of 100 depleted small dust (bottom) for C/O ratios of 0.47, 1.0, and 2.0 (left to right).

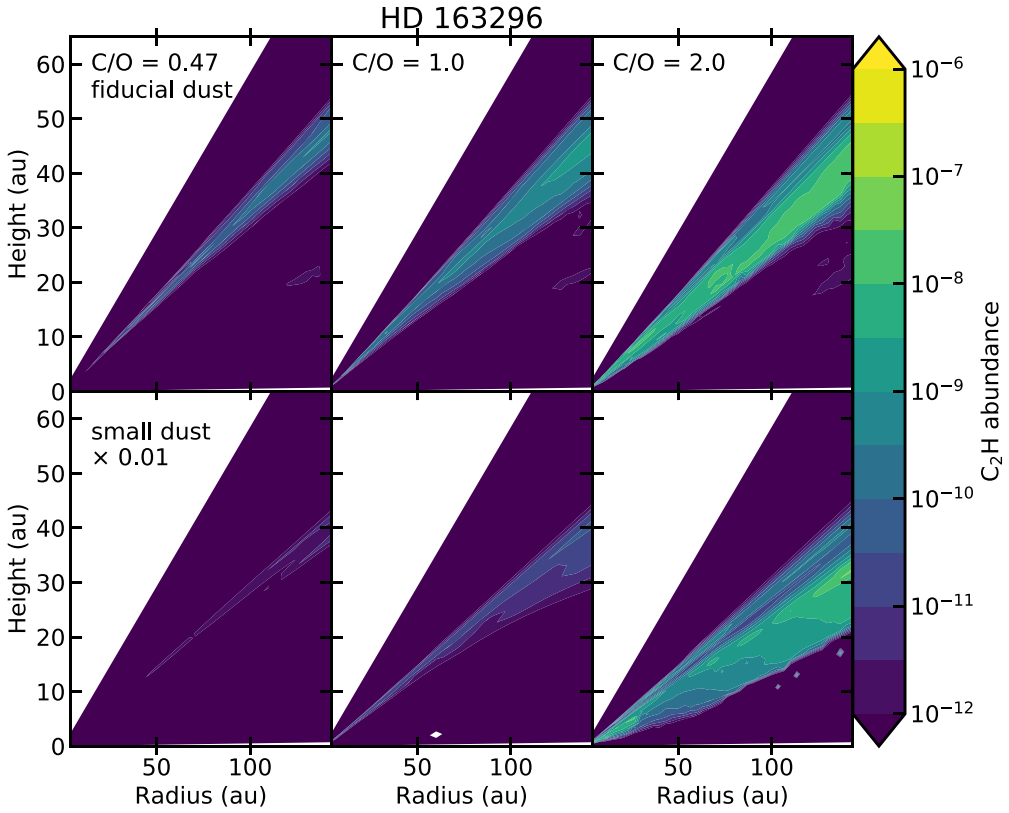

Figure 7. Same as Figure 6 but for HD 163296.

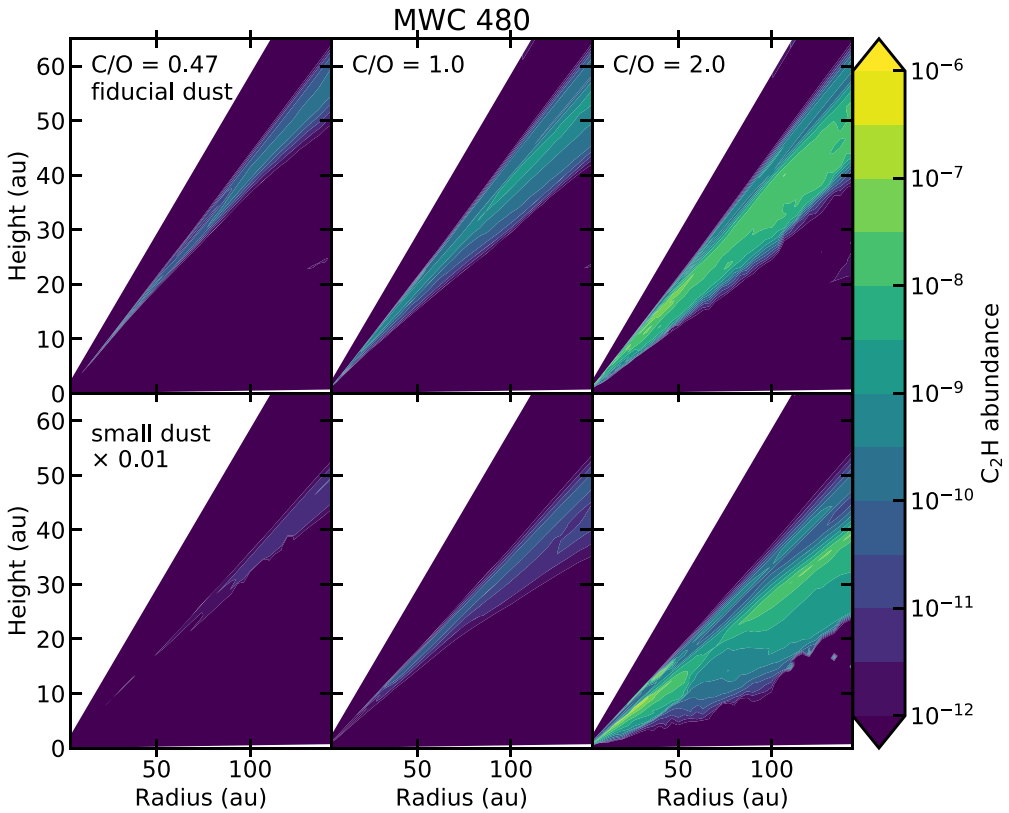

Figure 8. Same as Figure 6 but for MWC 480.

ORCID iDs

Arthur D. Bosman https://orcid.org/0000-0003-4001-3589
Felipe Alarcón https://orcid.org/0000-0002-2692-7862
Edwin A. Bergin https://orcid.org/0000-0003-4179-6394
Ke Zhang https://orcid.org/0000-0002-0661-7517
Merel L. R. van't Hoff https://orcid.org/0000-0002-2555-9869
Karin I. Öberg https://orcid.org/0000-0001-8798-1347
Viviana V. Guzmán https://orcid.org/0000-0003-4784-3040
Catherine Walsh https://orcid.org/0000-0001-6078-786X
Yuri Aikawa https://orcid.org/0000-0003-3283-6884
Sean M. Andrews https://orcid.org/0000-0003-2253-2270
Jennifer B. Bergner https://orcid.org/0000-0002-8716-0482
Alice S. Booth https://orcid.org/0000-0003-2014-2121
Gianni Cataldi https://orcid.org/0000-0002-2700-9676
L. Ilsedore Cleeves https://orcid.org/0000-0003-2076-8001
Ian Czekala https://orcid.org/0000-0002-1483-8811
Kenji Furuya https://orcid.org/0000-0002-2026-8157
Jane Huang https://orcid.org/0000-0001-6947-6072
John D. Ilee https://orcid.org/0000-0003-1008-1142
Charles J. Law https://orcid.org/0000-0003-1413-1776
Romane Le Gal https://orcid.org/0000-0003-1837-3772
Yao Liu https://orcid.org/0000-0002-7616-666X
Feng Long https://orcid.org/0000-0002-7607-719X
Ryan A. Loomis https://orcid.org/0000-0002-8932-1219
François Ménard https://orcid.org/0000-0002-1637-7393
Hideko Nomura https://orcid.org/0000-0002-7058-7682
Chunhua Qi https://orcid.org/0000-0001-8642-1786
Kamber R. Schwarz https://orcid.org/0000-0002-6429-9457
Richard Teague https://orcid.org/0000-0003-1534-5186
Takashi Tsukagoshi https://orcid.org/0000-0002-6034-2892
Yoshihide Yamato https://orcid.org/0000-0003-4099-6941
David J. Wilner https://orcid.org/0000-0003-1526-7587

References

Aikawa, Y., Cataldi, G., Yamato, Y., et al. 2021, ApJS, 257, 13
Alarcón, F., Bosman, A. D., Bergin, E. A., et al. 2021, ApJS, 257, 8
Andrews, S. M., Huang, J., Pérez, L. M., et al. 2018, ApJL, 869, L41
Bergin, E. A., Du, F., Cleeves, L. I., et al. 2016, ApJ, 831, 101
Bergner, J. B., Öberg, K. I., Bergin, E. A., et al. 2020, ApJ, 898, 97
Bergner, J. B., Öberg, K. I., Guzmán, V. V., et al. 2021, ApJS, 257, 11
Bertin, M., Romanzin, C., Doronin, M., et al. 2016, ApJL, 817, L12
Booth, R. A., Clarke, C. J., Madhusudhan, N., & Ilee, J. D. 2017, MNRAS, 469, 3994
Booth, R. A., & Ilee, J. D. 2019, MNRAS, 487, 3998
Bosman, A. D., Alarcón, F., Zhang, K., & Bergin, E. A. 2021, ApJ, 910, 3
Bosman, A. D., Banzatti, A., Bruderer, S., et al. 2019, A&A, 631, A133
Bosman, A. D., Bergin, E. A., Loomis, R. A., et al. 2021, ApJS, 257, 15
Bosman, A. D., Walsh, C., & van Dishoeck, E. F. 2018, A&A, 618, A182
Bruderer, S. 2013, A&A, 559, A46
Bruderer, S., van Dishoeck, E. F., Doty, S. D., & Herczeg, G. J. 2012, A&A, 541, A91
Calahan, J., Bergin, E. A., Zhang, K., et al. 2021, ApJS, 257, 17
Ciesla, F. J. 2010, ApJ, 723, 514
Ciesla, F. J., & Cuzzi, J. N. 2006, Icar, 181, 178
Cleeves, L. I., Adams, F. C., & Bergin, E. A. 2013, ApJ, 772, 5
Cleeves, L. I., Öberg, K. I., Wilner, D. J., et al. 2018, ApJ, 865, 155
Cridland, A. J., Bosman, A. D., & van Dishoeck, E. F. 2020, A&A, 635, A68
Cridland, A. J., Pudritz, R. E., Birnstiel, T., Cleeves, L. I., & Bergin, E. A. 2017, MNRAS, 469, 3910
Draine, B. T., & Bertoldi, F. 1996, ApJ, 468, 269
Du, F., & Bergin, E. A. 2014, ApJ, 792, 2
Eistrup, C., Walsh, C., & van Dishoeck, E. F. 2016, A&A, 595, A83
Furuya, K., & Aikawa, Y. 2014, ApJ, 790, 97
Garrod, R. T., Widicus Weaver, S. L., & Herbst, E. 2008, ApJ, 682, 283
Garufi, A., Quanz, S. P., Schmid, H. M., et al. 2014, A&A, 568, A40
Gravity Collaboration, Nowak, M., Lacour, S., et al. 2020, A&A., 633, A110
Greene, T. P., Line, M. R., Montero, C., et al. 2016, ApJ, 817, 17
Guzmán, V. V., Bergner, J. B., Law, C. J., et al. 2021, ApJS, 257, 6
Guzmán, V. V., Huang, J., Andrews, S. M., et al. 2018, ApJL, 869, L48
Harsono, D., Bruderer, S., & van Dishoeck, E. F. 2015, A&A, 582, A41
He, J., & Vidali, G. 2014, ApJ, 788, 50
Heays, A. N., Bosman, A. D., & van Dishoeck, E. F. 2017, A&A, 602, A105
Huang, J., Bergin, E. A., Öberg, K. I., et al. 2021, ApJS, 257, 19
Huang, J., Andrews, S. M., Dullemond, C. P., et al. 2018, ApJL, 869, L42
Hunter, J. D. 2007, CSE, 9, 90
Ilee, J. D., Forgan, D. H., Evans, M. G., et al. 2017, MNRAS, 472, 189
Isella, A., Huang, J., Andrews, S. M., et al. 2018, ApJL, 869, L49
Jansen, D. J., Spaans, M., Hogerheijde, M. R., & van Dishoeck, E. F. 1995, A&A, 303, 541
Johnson, J. A., Aller, K. M., Howard, A. W., & Crepp, J. R. 2010, PASP, 122, 905
Kamp, I., & Bertoldi, F. 2000, A&A, 353, 276
Krijt, S., Bosman, A. D., Zhang, K., et al. 2020, ApJ, 899, 134
Krijt, S., & Ciesla, F. J. 2016, ApJ, 822, 111
Lagrange, A. M., Rubini, P., Nowak, M., et al. 2020, A&A, 642, A18
Lavie, B., Mendonça, J. M., Mordasini, C., et al. 2017, AJ, 154, 91
Law, C., Loomis, R. A., Teague, R., et al. 2021a, ApJS, 257, 3
Law, C., Teague, R., Loomis, R. A., et al. 2021b, ApJS, 257, 4
Liu, Y., Dipierro, G., Ragusa, E., et al. 2019, A&A, 622, A75
Long, F., Pinilla, P., Herczeg, G. J., et al. 2018, ApJ, 869, 17
Long, F., Herczeg, G. J., Harsono, D., et al. 2019, ApJ, 882, 49
Madhusudhan, N. 2019, ARA&A, 57, 617
Madhusudhan, N., Bitsch, B., Johansen, A., & Eriksson, L. 2017, MNRAS, 469, 4102
Madhusudhan, N., Knutson, H., Fortney, J. J., & Barman, T. 2014, in Protostars and Planets VI, ed. H. Beuther et al. (Tucson: Univ. Arizona Press), 739
Mawet, D., Absil, O., Montagnier, G., et al. 2012, A&A, 544, A131
McElroy, D., Walsh, C., Markwick, A. J., et al. 2013, A&A, 550, A36
Miotello, A., Facchini, S., van Dishoeck, E. F., et al. 2019, A&A, 631, A69
Monnier, J. D., Harries, T. J., Aarnio, A., et al. 2017, ApJ, 838, 20
Morbidelli, A., Szulágyi, J., Crida, A., et al. 2014, Icar, 232, 266
Mordasini, C., Alibert, Y., & Benz, W. 2009, A&A, 501, 1139
Muro-Arena, G. A., Dominik, C., Waters, L. B. F. M., et al. 2018, A&A, 614, A24
Nagy, Z., Ossenkopf, V., Van der Tak, F. F. S., et al. 2015, A&A, 578, A124
Noble, J. A., Congiu, E., Dulieu, F., & Fraser, H. J. 2012, MNRAS, 421, 768
Öberg, K. I., & Bergin, E. A. 2021, PhR, 893, 1
Öberg, K. I., Boogert, A. C. A., Pontoppidan, K. M., et al. 2011, ApJ, 740, 109
Öberg, K. I., Garrod, R. T., van Dishoeck, E. F., & Linnartz, H. 2009a, A&A, 504, 891
Öberg, K. I., Guzmán, V. V., Walsh, C., et al. 2021, ApJS, 257, 1
Öberg, K. I., Linnartz, H., Visser, R., & van Dishoeck, E. F. 2009b, ApJ, 693, 1209
Öberg, K. I., van Dishoeck, E. F., & Linnartz, H. 2009c, A&A, 496, 281
Paardekooper, S. J., & Mellema, G. 2006, A&A, 453, 1129
Penteado, E. M., Walsh, C., & Cuppen, H. M. 2017, ApJ, 844, 71
Pinte, C., Ménard, F., Duchêne, G., et al. 2018, A&A, 609, A47
Piso, A.-M. A., Öberg, K. I., Birnstiel, T., & Murray-Clay, R. A. 2015, ApJ, 815, 109
Rosotti, G. P., Juhasz, A., Booth, R. A., & Clarke, C. J. 2016, MNRAS, 459, 2790
Schwarz, K. R., Bergin, E. A., Cleeves, L. I., et al. 2016, ApJ, 823, 91
Schwarz, K. R., Calahan, J. K., Zhang, K., et al. 2021, ApJS, 257, 20
Shakura, N. I., & Sunyaev, R. A. 1973, A&A, 24, 337
Sierra, A., Pérez, L. M., Zhang, K., et al. 2021, ApJS, 257, 14
Sing, D. K., Fortney, J. J., Nikolov, N., et al. 2016, Natur, 529, 59
Tanigawa, T., Ohtsuki, K., & Machida, M. N. 2012, ApJ, 747, 47
Teague, R., Bae, J., Aikawa, Y., et al. 2021, ApJS, 257, 18
Teague, R., Bae, J., & Bergin, E. A. 2019, Natur, 574, 378
Teague, R., Bae, J., Bergin, E. A., Birnstiel, T., & Foreman-Mackey, D. 2018, ApJL, 860, L12
Todorov, K. O., Line, M. R., Pineda, J. E., et al. 2016, ApJ, 823, 14
Trapman, L., Miotello, A., Kama, M., van Dishoeck, E. F., & Bruderer, S. 2017, A&A, 605, A69
van der Walt, S., Colbert, S. C., & Varoquaux, G. 2011, CSE, 13, 22
van Dishoeck, E. F., & Black, J. H. 1988, ApJ, 334, 771

Virtanen, P., Gommers, R., Oliphant, T. E., et al. 2020, NatMe, 17, 261
Visser, R., Bruderer, S., Cazzoletti, P., et al. 2018, A&A, 615, A75
Visser, R., van Dishoeck, E. F., & Black, J. H. 2009, A&A, 503, 323
Walsh, C., Nomura, H., & van Dishoeck, E. 2015, A&A, 582, A88
Welbanks, L., Madhusudhan, N., Allard, N. F., et al. 2019, ApJL, 887, L20
Winn, J. N., & Fabrycky, D. C. 2015, ARA&A, 53, 409
Zhang, K., Bergin, E. A., Blake, G. A., Cleeves, L. I., & Schwarz, K. R. 2017, NatAs, 1, 0130
Zhang, K., Booth, A. S., Law, C. J., et al. 2021, ApJS, 257, 5
Zhang, K., Bosman, A. D., & Bergin, E. A. 2020a, ApJL, 891, L16
Zhang, K., Schwarz, K. R., & Bergin, E. A. 2020b, ApJL, 891, L17
Zhang, S., Zhu, Z., Huang, J., et al. 2018, ApJ, 869, L47